SIMULATING IN-SITU CONDITIONS
FOR DIGITAL CORE ANALYSIS

S. Linden[1,2], T. Cvjetkovic[2], E. Glatt[2], J.-O. Schwarz[2] and A. Wiegmann[2]
[1]Fraunhofer ITWM, Fraunhofer-Platz 1, 67665 Kaiserslautern, Germany
[2]Math2Market GmbH, Stiftsplatz 5, 67655 Kaiserslautern, Germany

ABSTRACT

Digital rock physics (DRP) for routine and special core analysis is usually based on 3D digital images acquired under ambient conditions. Hence it does not account for the pressure release the rocks suffer during the uplift from reservoir to laboratory conditions. The resulting change in the pore space affects all physical properties significantly. In this paper we present an efficient workflow to perform the full digital core analysis under in-situ conditions. The in-situ conditions are modeled by numerically compressing a scan taken under ambient conditions rather than performing the scan under in-situ conditions. The workflow is illustrated using a segmented 3D image of a Berea sandstone derived from a CT-scan under ambient conditions. Our results confirm that high geostatic pressures lead to significant changes of the physical rock properties.

INTRODUCTION

In the oil and gas industry, digital rock physics (DRP) on 3D images is a fast growing research topic. It is a standard tool to supplement and replace routine core analysis (RCA) and special core analysis (SCAL). However, most simulations are performed on 3D images taken under ambient conditions by μCT or FIB-SEM. The uplift of rocks from high geostatic pressures to ambient conditions enlarges the overall pore space. This change in pore space affects all physical properties significantly and has to be taken into account. Another challenge for DRP is the need to work on representative elementary volumes (REV) and hence very large images due to the inhomogeneity of the samples. In this paper we study the influence of increasing the geostatic pressure on

1. Porosity & pore size distributions,
2. Absolute & relative permeability,
3. Electrical conductivity, resistivity index & formation factor and
4. Capillary pressure.

There are two approaches to simulate in-situ conditions: (i) performing a scan under in-situ conditions or (ii) numerically compressing a scan taken under ambient conditions. We present an efficient workflow that allows computing these properties under in-situ conditions by numerically compressing a scan. The simulations are performed using the digital material laboratory GeoDict. Its built-in highly optimized numerical solvers are

capable of performing simulations on very large REVs (e.g. 1000³ voxels). The workflow is illustrated using a segmented 3D image of Berea sandstone [1, 2] derived from a CT-scan under ambient conditions.

METHODS
The physical properties mentioned above are computed on 3D digital images that may stem from µCT-scans, FIB-SEM, or virtual rock models. The outline of the proposed workflow is

1. Acquisition of µCT-scans or FIB-SEM images under ambient conditions
2. Segmentation of the image into solid phases and pore space
3. Numerical compression of the 3D image (NEW STEP)
4. Computation of single-phase properties
    a. Porosity & pore size distributions
    b. Absolute permeability
    c. Electrical conductivity and formation factor
5. Computation of the distribution of the two liquid phases in the pore space
6. Computation of two-phase properties on varying saturation states
    a. Capillary pressure
    b. Resistivity index
    c. Relative permeability

The calculations are performed by highly optimized numerical solvers that work directly on 3D digital images, without additional meshing. It is also not required to assemble matrices that describe discretized physical equations. That approach reduces the memory consumption dramatically. All but one solver use Fourier transforms to reduce the number of iterations, and thus achieve very low runtimes.

Numerical compression
The prediction of mechanical properties and the geostatic correction, i.e. uniaxial compression of the sample, is computed with the FeelMath [3,4] solver. The input parameter for the compression step is the compression rate in percent or a given geostatic pressure. In this section we summarize the basic ideas of the implemented algorithms.

The equations of linear elasticity for a constant macroscopic strain S are defined by

$$\nabla \cdot \sigma = 0 \qquad \qquad Equilibrium$$
$$\sigma = C : \epsilon \qquad \qquad Hooke's\ law \qquad (1)$$
$$2\epsilon = 2S + \nabla u^* + (\nabla u^*)^T$$

for the stress-field σ, strain-field ϵ, and the displacement-field u^*. By introducing a reference material of homogeneous stiffness C^0 these equations can be reformulated into the Lippmann Schwinger equation

$$\epsilon + \Gamma^0 * \left((C - C^0) : \epsilon \right) = S \qquad (2)$$

where the convolution of the Green operator Γ^0 can be solved by using Fast Fourier transforms. The solver is able to handle linear and non-linear (i.e. replacing Hooke's law with a non-linear formulation) material laws assigned to mineral phases. The number of iterations required for computation depends on the largest phase contrast in the structure.

Then the displacement field u^* is used to predict a compressed structure [5]. The voxels of the original image are moved along the displacement field and cut with a reduced boxel image. The size of the boxel image can be derived from the input parameters. The result of that procedure is a gray-value image where a global threshold is used to perform a segmentation of the different phases. The threshold is chosen such that either mass or volume is preserved. Then the boxel image is resampled to a voxel image again.

For the mechanical properties it is important to capture the complete mineralogy in the segmentation process to predict representative results. Another important aspect to improve the validity is the correct modelling of contacts between grains. The stiffness at grain-to-grain interfaces is much lower compared to the stiffness within the grains. We approximate that aspect with an increased uniaxial macroscopic stress. The compressed 3D image is then used in further computations of the workflow.

Distribution of the Two Liquid Phases
The pore morphology method [6], also known as method of maximal inscribed spheres [7] predicts the distribution of a wetting phase (WP) and a non-wetting phase (NWP) inside a porous medium. The method distributes the phases by using morphological operations rather than solving partial differential equations. For drainage, spheres that represent the NWP are placed inside the pore space where the pore size is greater than a certain radius. The radius is decreased in an iterative process, i.e. the capillary pressure is increased. Additional connectivity checks with respect to NPW and WP reservoirs can be used to increase the validity of the distributions. These connectivity checks allow the algorithm to introduce residual phases where parts of the NWP are trapped and cannot leave the simulated domain.

The output of the algorithm is a finite sequence of quasi-stationary states. Each state is a 3D image again that encodes the solid phase, WP and NWP. In a post-processing step the Young-Laplace equation based on the radii of the inscribed spheres and the interfacial tension is used to predict the capillary pressure curve. The sequence of 3D images is then the input data to predict relative properties.

Absolute and Relative Permeability
Absolute and relative permeability on the WP and NWP are computed with the SIMPLE-FFT and LIR-Stokes [8] methods. The SIMPLE-FFT is an enhancement of the original SIMPLE algorithm that solves the pressure correction within a single step using Fourier transforms. The LIR-Stokes solver uses an adaptive tree structure and solves the

discretized Stokes equations at once for each cell. The methods are very fast and in particular the latter has very low memory requirements.

Both methods assume no-slip boundary conditions at pore-solid interfaces for the absolute permeability and also no-slip boundary conditions at WP-NWP interfaces for the relative permeability. At the domain boundaries we assume periodic boundary condition with inlet (e.g. 16 voxel) in flow direction. This flow boundary condition connects all pores from inlet and outlet and predicts permeabilities between those of purely periodic boundary conditions and symmetry boundary conditions.

Electrical Conductivity and Resistivity Index

The electrical conductivity, resistivity index and formation factor are computed with the Explicit Jump Immersed Interface Method [9, 10]. Additional jump variables at material interfaces are introduced to represent discontinuities inside the flux. The physical problem can be reformulated from a three-dimensional to a two-dimensional problem where the method solves for the jump variables. The number of iterations depends on the number of interfaces. The chosen boundary conditions for the electrical properties are similar to the flow properties. For the resistivity index we also assume that the NWP is non-conductive.

RESULTS

In our experiments we use a binary segmented 3D image of a computed tomography scan from a Berea sandstone under ambient conditions. The image consists of 720 x 720 x 1024 voxels, has a resolution of 0.74 µm, and is shown in Figure 1 together with the original gray value image. The origin and segmentation of the dataset is described in the first part of the benchmark study [1]. The second part of the benchmark study [2] includes the numerical computation of physical properties but considers permeability, electric conductivity and elastic moduli only.

Table 1 shows runtimes and memory consumptions for single computations of the numerical solvers. Depending on the available computational resources, all simulations can be performed in a couple of days. Figure 5 shows the graphs of porosity, pore sizes, formation resistivity factor, absolute permeability, capillary pressure, and resistivity index with respect to the pressure states.

Mechanical Properties and Numerical Compression

First, we compute a sequence of images which have been corrected for different geostatic pressures, i.e. numerical compression with the states: 0.0, 0.12, 0.24, 0.48, 0.71, 0.95, and 1.43 GPa. Pores are assumed to be filled with air ($E = 0$ GPa and $\nu = 0$) and the solid phase is assumed to be quartz ($E = 94.5$ GPa and $\nu = 0.074$). Then the core analysis is performed on each compression step. The pressures correspond to the compression ratios: 0.0, 0.25, 0.5, 1.0, 1.5, and 3.0%. The computed isotropic elastic modulus is E = 45.9 GPa and the Poisson ratio is $\nu = 0.108$ for the uncompressed Berea sandstone. The visible

difference of the uncompressed and compressed image can be seen in Figure 2 and indicates a significant change of effective physical properties.

Porosity and Pore Size Distribution
The porosity of the uncompressed sample is 18.4 % and decreases linearly to 15.7 %. The (relative) pore size distribution (PSD) obtained by maximum inscribed spheres does not change significantly under increasing geostatic pressure. In contrast to the Porosimetry simulation where the most frequent pore diameter 8.8 µm is decreased to 7.4 µm. A reduction between 2% and 3% is a reasonable value for sandstone and agrees with measured values in literature [12].

Absolute Permeability
The absolute permeability is 108 mD under ambient conditions and decreases with a high slope to 66 mD under in-situ conditions. This decline of permeability agrees with the relation of velocity and pore diameter. Figure 3 shows the velocity field of a Stokes flow under ambient conditions. The trend agrees to the measured stress dependence of permeability reported in [12].

Absolute Electrical Conductivity and Formation Factor
The electrical conductivity of the fully Brine saturated Berea sandstone is simulated to 0.17 S/m, assuming that Brine has a conductivity of 5 S/m and Quartz is non-conductive. Figure 3 shows the potential field for the fully saturated medium under ambient conditions. The corresponding formation resistivity factor increases almost linear from 27 to 39 when air drains brine as illustrated in Figure 4. That behavior coincides with the linear decrease of the pore diameters.

In contrast to the permeability, the number of iterations for computing electrical properties is almost the same from ambient to in-situ conditions. This can be explained by the fact that the number of iterations depends on the brine surface area which does not change significantly during the numerical compression.

Two-Phase Distribution
The pore morphology method is used to perform a drainage simulation. Figure 4 shows different stationary saturation states of the drainage process where air drains brine. In that experiment we assumed a non-wetting phase (Air) reservoir at the top and a wetting phase (Brine) reservoir at the bottom of the domain.

Since that method does not solve a partial differential equation the computation is much faster compared to the computations of single-phase flow, mechanical, and electrical properties. A subset of these quasi stationary states is used to predict relative properties.

Capillary Pressure
Similar to the pore size distribution, the capillary pressure curve computed from the two-phase distribution does not change significantly within the investigated geostatic pressure

range. The irreducible wetting phase saturation is 17.3% but the displacement pressure increases from 24 kPa to 29 kPa.

Relative Permeability
The relative permeability of the wetting phase is almost the same for ambient and in-situ conditions other than the relative permeability of the non-wetting phase. Figure 6 shows the relative permeability of both phases with respect to the normalized wetting phase. The decline occurs more early and can be explained by delayed breakthrough of the non-wetting phase.

The relative permeability is the most expensive property to compute depending on the number of saturation states. The number of iterations increases significantly in lower saturation states even though the number of computational cells decreases. The SIMPLE-FFT method cannot profit from the decreasing number of cells while the LIR method can and hence the runtime per iteration decreases.

The number of iterations needed until the same stopping criterion is reached increases by 25% for computing the absolute permeability from ambient to in-situ conditions. This can be explained by the increased complexity of the pore space. That behavior can be observed for the SIMPLE-FFT, LIR, and also other flow solvers.

Resistivity Index
The electrical conduction simulation is performed for the wetting phase on 8 saturation states from 0.3 to 1.0. Figure 5 shows the resistivity index for the Berea sandstone under ambient and in-situ conditions together with an exponential fitting curve. The saturation exponents of Archie's law are 2.38 and 2.04, respectively. Similar to the relative permeability, the absolute resistivity of the wetting phase under ambient condition is greater compared to the in-situ conditions.

CONCLUSION
The integrated approach of highly optimized solver technologies allows performing the full digital core analysis under in-situ conditions in a short amount of time and memory. Our results confirm that high geostatic pressure leads to different physical rock properties. The impact is significant on the single-phase properties: porosity, the most frequent pore diameter, permeability, and formation factor. The capillary pressure, resistivity index, and relative permeability are also influenced by increasing pressure but to a lesser extent. The next step is a comparative study of digital and laboratory in-situ conditions, also for other types of rocks. In addition, numerical simulations and modelling will be improved in at least three ways: 1. segmentation of all mineral phases, 2. modelling and consideration of grain contacts, and 3. improving the computational runtimes for relative properties.

REFERENCES

1. H. Andrä, N. Combaret, J. Dvorkin, E. Glatt, H. Junehee, M. Kabel, Y. Keehm, F. Krzikalla, M. Lee, C. Madonna, M. Marsh, T. Mukerji, E. Saenger, R. Sain, N. Saxena, S. Ricker, A. Wiegmann and X. Zhan, "Digital rock physics benchmarks Part I: Imaging and segmentation," Computers & Geosciences, 2013 (43), pp. 25-32.
2. H. Andrä, N. Combaret, J. Dvorkin, E. Glatt, H. Junehee, M. Kabel, Y. Keehm, F. Krzikalla, M. Lee, C. Madonna, M. Marsh, T. Mukerji, E. Saenger, R. Sain, N. Saxena, S. Ricker, A. Wiegmann and X. Zhan, "Digital rock physics benchmarks Part II: Computing effective properties," Computers & Geosciences, 2013 (43), pp. 33-43.
3. M. Kabel and H. Andrä, Fast numerical computation of precise bounds of effective, Report of Fraunhofer ITWM, 2013 (224).
4. M. Kabel, T. Böhlke and M. Schneider, "Efficient fixed point and Newton-Krylov solvers for FFT-based homogenization of elasticity at large deformations," Computational Mechanics, 2014 (54), pp. 1497-1514.
5. M. Kabel, H. Andrä, F. Hahn and M. Lehmann, "Simulating the Compression of Filter Materials," Proceedings of FILTECH, 2013
6. M. Hilpert and C. T. Miller, "Pore-morphology-based simulation of drainage in totally wetting porous media," Advances in Water Resources, 2001 (24), pp. 243-255.
7. D. Silin, L. Tomutsa, S.M. Benson and T.W. Patzek, "Microtomography and Pore-Scale Modeling of Two-Phase Distribution," Transport in Porous Media, 2011 (86), pp. 495-515.
8. S. Linden, A. Wiegmann and H. Hagen, "The LIR space partitioning system applied to the Stokes equations," Dagstuhl Geometric Modelling 2014 Special Issure of Graphical Models, to be published.
9. A. Wiegmann and K. P. Bube, "The Explicit-Jump immersed interface method: Finite difference methods for PDE with piecewise smooth solutions," SIAM Journal on Numerical Analysis, 2000 (37 No 3), pp. 827-862.
10. A. Wiegmann and A. Zemitis, "EJ-Heat: A fast Explicit-Jump harmonic averaging solver for the effective heat conductivity of composite materials," Fraunhofer ITWM Technical Report No 94, 2006.
11. J.J. Dong, J.Y. Hsu, W.J. Wu, T. Shimamoto, J.H. Hung, E.C. Ye, Y.H. Wu and H. Sone, "Stress-dependence of the Permeability and Porosity of Sandstone and Shale from TCDP Hole-A," International Journal of Rock Mechanics and Mining Sciences, 2010 (47), pp. 1141-1157
12. S. Linden, T. Cvjetkovic, E. Glatt and A. Wiegmann, "An integrated approach to compute physical properties of core samples," Proceedings of SCA Avignon, 2014, Paper 057.

FIGURES AND TABLES

Table 1 Runtime and Memory requirements of the solvers on a computer with 16 cores and 128 GB RAM. The runtimes account for a single simulation on the uncompressed Berea sandstone.

Method	Flow (SIMPLE-FFT)	Flow (LIR)	Electrical Conduction (Explicit Jump)	Two-Phase Distribution (Pore Morphology)	Mechanics (FeelMath)
Runtime [h]	3.6	3.1	0.6	0.8	8.3
Memory [GB]	42.3	5.4	9.4	5.0	97.1
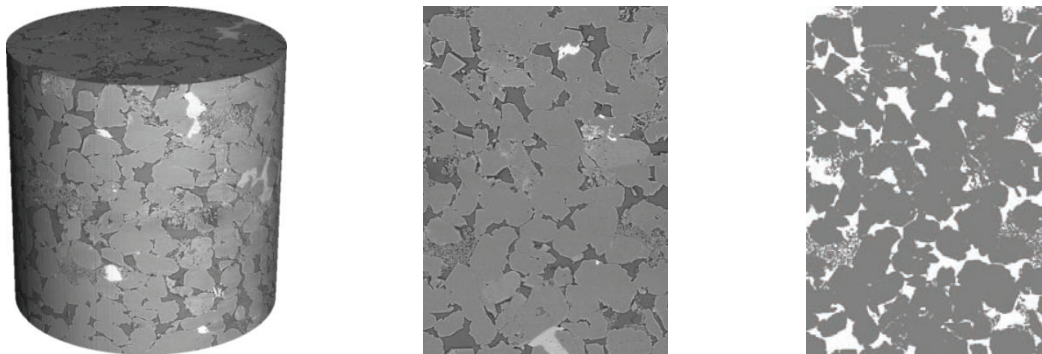
Figure 1 Gray value image from the Berea sandstone (left and center) with a binary segmentation (right). The gray value image consists of 1024x1024x1024 voxel and the cropped segmentation consists of 720x720x1024 voxel.

Figure 2 Cut-out from the segmented image of Berea sandstone before (left) and after (right) numerical compression (1.43 GPa). The pore diameter in the blue region is visibly decreased while even the connectivity of the pores is reduced in the two red regions.
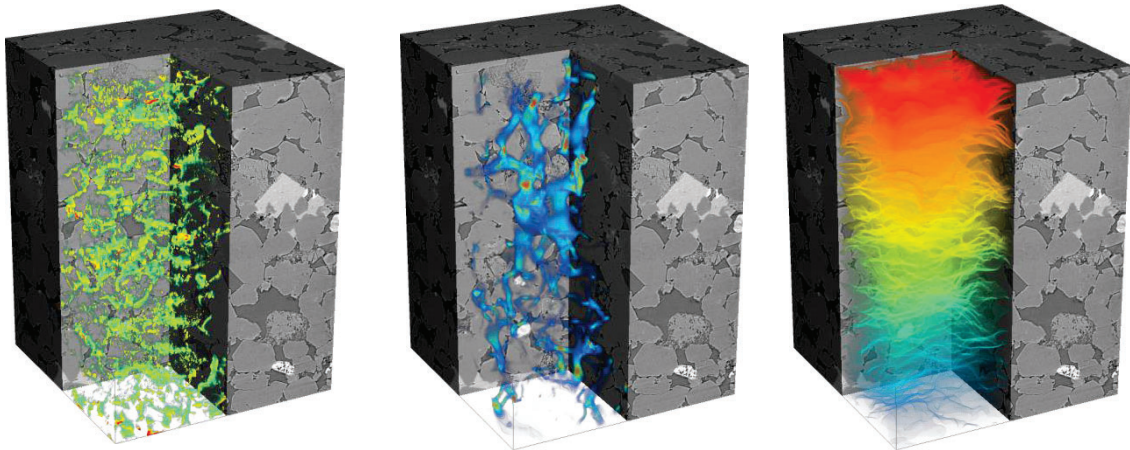
Figure 3 Visualization of the von-Mises stress (left), the velocity field of a Stokes flow (center) and electrical potential (right) on a smaller cut-out. A compression, drop in pressure, and potential difference are applied in y-direction from top to bottom.
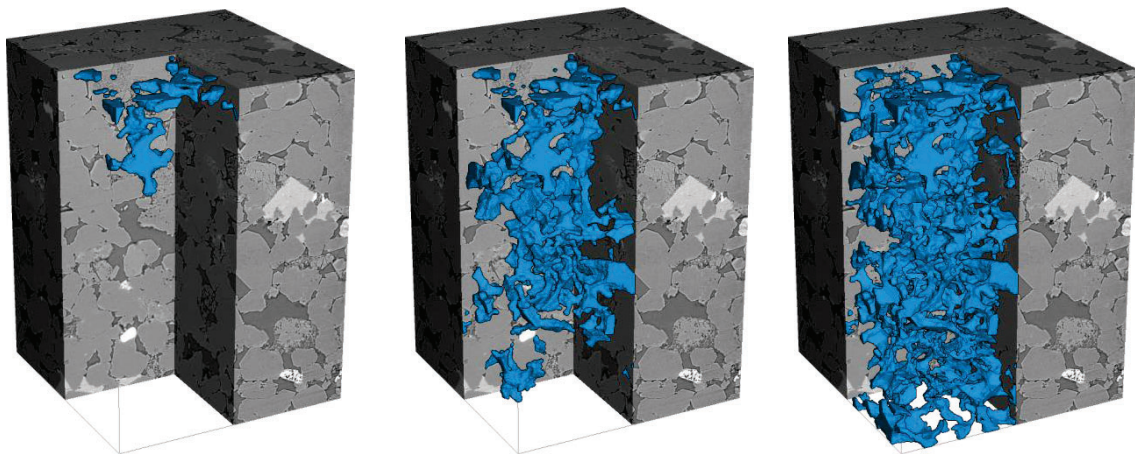

Figure 4 Air drains brine and we visualize air saturations of 25%, 50% and 75% respectively.
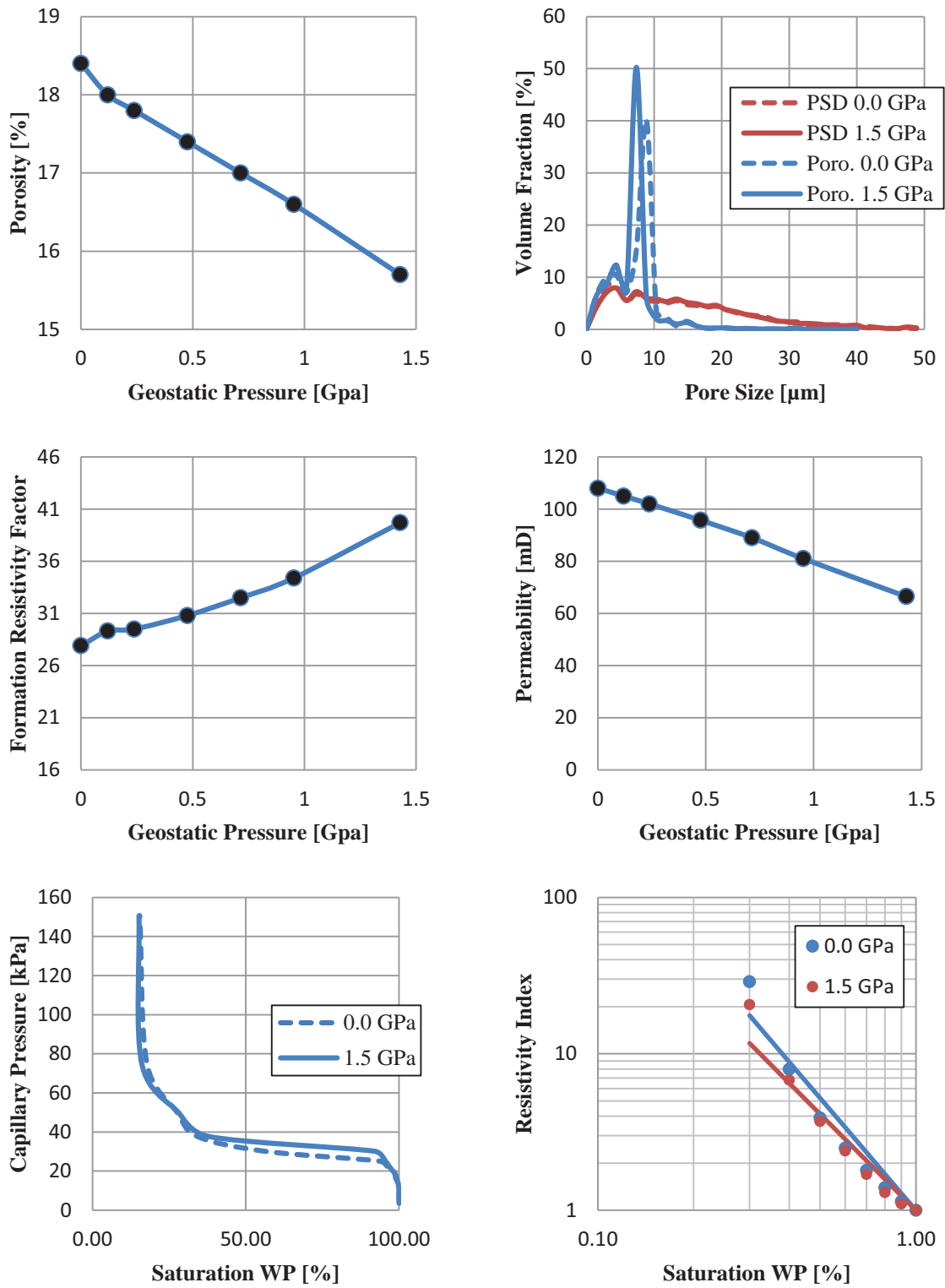
Figure 5 Porosity, pore size distribution, porosimetry, formation resistivity factor, absolute permeability, capillary pressure, and resistivity index for different applied geostatic pressures.
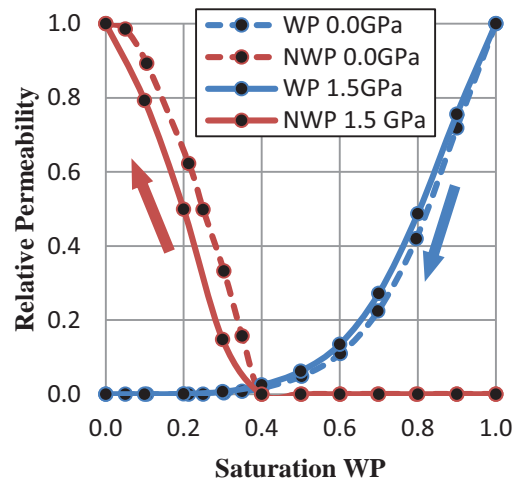
Figure 6 Relative permeability of the WP and NPW for ambient and in-situ conditions.